PAPER

Check for updates

Optoelectronic and photovoltaic assessment of Na₂ReAlO₆ double perovskite: insights from DFT and SCAPS modeling

Sanober Kanwal,[a] Ahsan Illahi,*[a] Muhammad Kaleem, [b] Amna Nasir,[b] M. Anis-ur-Rehman[c] and Muhammad Tanzeel[b]

The recent progress in oxide double perovskite (DP) based perovskite solar cells (PSCs) has driven extensive research aimed at enhancing device performance owing to their remarkable optoelectronic properties. The oxide double perovskite Na₂ReAlO₆ has emerged as a promising Pb-free alternative to conventional lead-based absorbers due to its reduced toxicity, enhanced chemical stability, and favorable optoelectronic characteristics. In order to explore the structural, electronic, and optical behavior of Na₂ReAlO₆, density functional theory calculations were carried out using the full-potential linearized augmented plane wave (FP-LAPW) method in conjunction with the Tran–Blaha modified Becke–Johnson potential (TB-mBJ) and PBE-GGA within the Wien2K framework. A favorable tolerance factor and a phonon dispersion profile devoid of imaginary frequencies validate structural and dynamical stability. The material is suitable for photovoltaic (PV) and energy-related applications due to its direct bandgap of 1.24 eV with noble electrical stability and pronounced visible-light absorption (10^4 cm^{-1}) and high dielectric constant, indicating suitability for efficient solar energy conversion. Further SCAPS-1D (Solar Cell Capacitance Simulator in one dimension) was used to simulate the PV performance of Na₂ReAlO₆-based solar cell designs. The optimized structure of Na₂ReAlO₆ was integrated into heterostructured PSCs using CSTO and ZnS as electron transport layers (ETLs) and Cu₂O as the hole transport layer (HTL) are optimized to demonstrate the photovoltaic features of simulated PSCs delivering a power conversion efficiency (PCE) up to 29%. These findings demonstrate the device-level potential of Na₂ReAlO₆ for Pb-free PSCs as a stable, non-toxic and extremely effective oxide DP absorber.

1. Introduction

The rapid depletion of fossil fuels and the rising global energy demand have sped up the search for sustainable and environmentally friendly energy sources.[1–3] One essential requirement for such renewable energy devices is the capacity to convert heat or solar energy into electrical energy. Cost, safety and efficiency are the three main factors that determine the choice of material. Researchers are interested in double perovskite materials because of their fascinating applications in optoelectronics, thermoelectricity and energy storage devices.[4] Over the past ten years lead-based double perovskites' efficiency has greatly grown. Researchers are now interested in their toxicity and stability due to this notable increase in efficacy.[5] However their toxicity is the main reason they are harmful to the ecosystem.

Finding lead-free double perovskite materials that are suitable for the environment is therefore essential. Perovskite oxides have recently gained popularity due to their remarkable qualities which include their high absorption coefficient, non-toxicity and good carrier transport. These characteristics make them ideal for solar cell applications.[6] For use in solar cells and optoelectronic devices, oxide perovskites have a significant advantage over halide perovskites due to their affordable price and excellent power conversion efficiency.[7]

Due to their exceptional structural tunability, multifunctional characteristics and chemical composition flexibility, double perovskite oxides with the general formula A_2YZO_6 have attracted a lot of attention.[8,9] The elementary AYO_3 perovskite in which two different cations (Y and Z) alternately occupy the Y-site is the source of the double perovskite structure with ordered and stable cubic or tetragonal symmetry. Among these materials' rich physical characteristics are ferroelectricity, thermoelectricity and strong light absorption.[10] Selectively substituting cations at the A- and Y-sites of materials is an effective way to modify structural and electrical properties that provide fine control over band gaps with magnetic ordering and optical absorption. Therefore, researching novel double perovskite

Research in Modeling and Simulation Group, Department of Physics, COMSATS University Islamabad, Islamabad, Pakistan. E-mail: ahsanillahi@comsats.edu.pk

bDepartment of Physics, International Islamic University H-10, Islamabad 44000, Pakistan

cApplied Thermal Physics Laboratory, Department of Physics, COMSATS University Islamabad, Islamabad, Pakistan

systems using Density Functional Theory (DFT) can significantly promote the development of efficient optoelectronic and energy-harvesting materials.[11]

The electrical and optical features of double perovskite Ba_2VMoO_6 were explored by Hnamte et al.[12] using first-principle calculations. They claimed that the substance was semi-metal and that optoelectronic devices may benefit from it at the Fermi level. In a different article, Ray et al. also theoretically examined the optical and electrical properties of Ba_2ScSbO_6 molecules.[13] They suggested that it may be useful for dielectric resonators and filters in microwave applications due to its large bandgap. For use in solar cells, double perovskites such as La_2NiMnO_6 (LNMO), $DyNiMnO_6$ (DNMO), and Lu_2NiMnO_6 (LNMO) have been investigated.[14] Recently, the possible uses of Pb_2ScBiO_6, another oxide-based perovskite, in solar cells have been examined using density functional theory.[15] Khan et al. studied the structural, optical, thermal and mechanical robustness of Ca_2TiXO_6 (X = Ge, Sn) double perovskites that display semiconducting band gaps (2.37 eV, 2.17 eV) and strong visible light absorption demonstrating their photovoltaic potential.[16]

Combining Re with inexpensive lightweight elements like sodium (Na) or aluminum (Al) could result in stable and commercially feasible materials for energy conversion applications. Rhenium-based double perovskites have not received much attention whereas Re (5d) offers strong hybridization with oxygen orbitals and with improve carrier mobility and optical absorption.[17,18] The presence of Re at the Y-site is expected to introduce additional d-orbital contributions near the Fermi level which are based on electronic structure calculations and previous reports facilitate enhanced electronic conductivity and charge carrier mobility. In contrast, the low formation energy and retained lattice integrity observed in comparable alkali-metal-based perovskite systems indicate that Na occupancy at the A-site predominantly contributes to structural stabilization.[19,20]

Adhering first principle calculations within DFT[21] to fully examine the structural, electrical, optical and dynamical characteristics of Na_2ReAlO_6 compound. The outcomes highlight Na_2ReAlO_6 remarkable optical functionality in the visible region of the spectrum which may be useful for a variety of applications due to its structural stability and an optimal band gap value. The behavior of Na-based oxide double perovskites upon light absorption is clarified in this work using DFT simulations. The investigation focuses on the Na_2ReAlO_6 compound in particular with the goal of analyzing their potential for the future including optical characteristics solar cell functioning and electronic characteristics with the aptitude to produce light. In order to calculate various solar cell specs and power conversion efficiency this work mainly integrates the SCAPS-1D simulation tool with the DFT technique. While several studies have explored oxide and double perovskite materials for optoelectronic and photovoltaic applications, a careful survey of the existing literature reveals no prior reports addressing the photovoltaic device modeling or SCAPS-1D-based performance evaluation of Na_2ReAlO_6. For the first time, this work correlates DFT-based structural and optoelectronic properties of Na_2ReAlO_6 with full solar cell device simulations, providing

a comprehensive assessment of its suitability as a solar absorber material.

Although combined DFT and SCAPS-1D approaches have been widely employed for high-efficiency solar cell analysis, their application to the Na_2ReAlO_6 double perovskite has not been previously reported. Therefore, this study applies DFT calculations to characterize Na_2ReAlO_6 and subsequently models its photovoltaic performance using the SCAPS-1D.

2. Research methodology

Density Functional Theory (DFT) based first principles calculations using the full-potential linearized augmented plane wave (FP-LAPW) technique as implemented in the Wien2K code to thoroughly explore the structural and optoelectronic features of Na_2ReAlO_6 double perovskites.[22–24] An energy cutoff defined by $RK_{max} = 7.0$ was employed for the expansion of wave functions and electronic densities, which was confirmed to ensure convergence of total energy and charge density. Convergence tests were performed by varying RK_{max} values, and negligible changes in total energy were observed beyond this cutoff. Structural optimization was first conducted to determine the equilibrium lattice parameters, atomic positions, and minimum total energy. The Perdew–Burke–Ernzerhof (PBE) method's Generalized Gradient Approximation (GGA) was used to handle the exchange-correlation potential.[25] The optimization procedure was continued until the composition total energy convergence threshold reached 10^{-3} Ry. As no slab geometries were employed, dipole-moment corrections and vacuum-related potential alignment procedures were not required. Long-range electrostatic interactions were inherently treated through periodic boundary conditions within density functional theory. The systems investigated were charge neutral, and no charged defect configurations were introduced; therefore, charge-neutralization schemes and electrostatic correction terms associated with charged defects were not applied. All calculations were carried out for the pristine bulk crystal using a 40-atom conventional unit cell under fully periodic boundary conditions. The calculations were performed using bulk periodic boundary conditions; therefore, no surface slab or thickness-dependent models were considered or tested in this study. To accurately represent the electrical structure and the band structure and density of states (DOS) calculations were performed using the Tran-Blaha modified Becke–Johnson (TB-mBJ) potential.[26] To guarantee high computational precision a Monkhorst–Pack k-mesh of $10 \times 10 \times 10$ was used producing about 1000 k-points within the first irreducible Brillouin zone. The selected k-point scheme ensures balanced sampling across all reciprocal lattice directions and accurate representation of electronic states within the first Brillouin zone. Furthermore, Quantum ESPRESSO[27] and Phonopy package were coupled to accomplish the phonon computations using the finite displacement approach.[28] Additionally Solar Cell Capacitance Simulator-one Dimension (SCAPS-1D) a reputable numerical tool frequently used for modeling charge transport and interfacial behavior in multilayer photovoltaic devices was employed to analyze the electrical properties of the suggested solar cell

topologies.[29,30] The simulated device architecture consists of a multilayer stack arranged as ITO/ETL/Na$_2$ReAlO$_6$/HTL/Anode. Indium tin oxide (ITO) acts as the transparent front contact allowing light transmission and electron collection. ZnS and CSTO were alternately employed as electron transport layers (ETLs) to facilitate efficient electron extraction from the absorber layer. Na$_2$ReAlO$_6$ serves as the main photoactive absorber where photon absorption and charge generation occur. Cu$_2$O functions as the hole transport layer (HTL), enabling effective hole extraction and transport toward the rear anode. By resolving the linked Poisson electron and hole continuity equations throughout the device layers SCAPS-1D calculates the essential photovoltaic parameters enabling a thorough evaluation of charge generation, transport and recombination processes. By using two different ETLs it was possible to directly compare the effects of ZnS and CSTO on charge separation and carrier collection efficiency within the Na$_2$ReAlO$_6$-based PSC structure which eventually provided information about material-dependent performance variations and possible optimization paths.

3. Results and discussion

3.1 DFT analysis

3.1.1 Structural features. The stability of the perovskite type oxide structure Na$_2$ReAlO$_6$ is essential for evaluating its potential for energy conversion and optoelectronic applications. The geometric optimization of the material is measured by the lattice constant 7.57 Å which has an impact on the compound structural stability and its optimized values are given in Table 1 and optimized crystal structure is depicted in Fig. 1(a). The energy-volume curve illustrated in Fig. 1(b) provide additional information about the structural stability of Na$_2$ReAlO$_6$. The equilibrium volume or the point at which the system energy is minimized is found about 740 a.u. for Na$_2$ReAlO$_6$ and is obtained by plotting the material total energy as a function of volume. These findings imply that higher lattice constant and lower formation energy of Na$_2$ReAlO$_6$ making it denser and more stable at its equilibrium volume. The energy volume relationship indicate that this materials is stable and have expedient structural characteristics for possible potential in a variety of devices.[31] To quantitatively analyze the structural stability of these materials the Goldschmidt tolerance factor (τ) a widely recognized metric for evaluating the stability of perovskite phases can be calculated by the following eqn (1) which compares the ionic radii of each ion in the structure:[29,32]

$$\tau_G = \frac{(R_A + R_O)}{\sqrt{2\left(\frac{R_Y + R_X}{2} + R_O\right)}} \tag{1}$$

where R_A stands for the Shannon ionic radii of the A-site cation Na (1.39 Å) and R_Y for the B-site cation Re (0.53 Å) and R_X for Al (0.535 Å) and R_O for oxygen (1.35 Å).[33] The computed tolerance factor for Na$_2$ReAlO$_6$ is 1.04 ensure that the material retain its perovskite structure under normal circumstances because it is within the range usually associated with stable perovskite phases ($0.8 < \tau < 1.1$).[34,35] The octahedral factor (μ) which indicates the degree of distortion of the octahedral coordination surrounding the Y-site cation is another significant element influencing the structural stability of perovskite materials. The octahedral factor can be calculated using the following eqn (2):[36]

$$\mu = \frac{\frac{R_y + R_X}{2}}{R_O} \tag{2}$$

The computed octahedral factor for Na$_2$ReAlO$_6$ ($\mu = 0.39$) lies within the range commonly associated with stable octahedral coordination in perovskite structures, indicating geometric and structural stability rather than mechanical or thermodynamic integrity. Low μ values are widely used as geometric descriptors to assess the suitability of ionic radii for forming stable BO$_6$ octahedra in perovskites.[37] Moreover, the formation energy, defined as the energy change associated with forming the compound from its constituent elements, is an essential indicator of thermodynamic stability. In this study, the formation energy was calculated using ground-state (0 K) total electronic energies obtained from density functional theory (DFT) calculations.[38] Negative formation energies imply that the material must be able to form naturally under normal conditions for practical synthesis and can be calculated by eqn (3):[39,40]

$$\Delta H_f\,(\text{Na}_2\text{ReAlO}_6) = \frac{E_{total} - (2E_{Na} + E_{Re} + E_{Al} + 6E_O)}{10} \tag{3}$$

The formation energy reported in eqn (3) corresponds to the static ground-state (0 K) total-energy difference between the compound and its constituent elements, neglecting vibrational, rotational, and translational contributions. Accordingly, the reported values represent thermodynamic stability at the electronic level rather than finite-temperature formation free energies. Long-range interactions such as van der Waals forces are not explicitly included beyond the GGA functional; however, their influence is expected to be minimal for the present ionic perovskite system, although minor effects on total energies and structural parameters cannot be completely excluded. The calculated formation energy of Na$_2$ReAlO$_6$ is -3.78 eV per atom, indicating thermodynamic stability at the electronic ground state and suggesting that the compound is energetically favorable and potentially experimentally realizable, making it a promising candidate for clean-energy and solar-cell applications.[31]

Table 1 Structural parameters of Na$_2$ReAlO$_6$ perovskite oxide

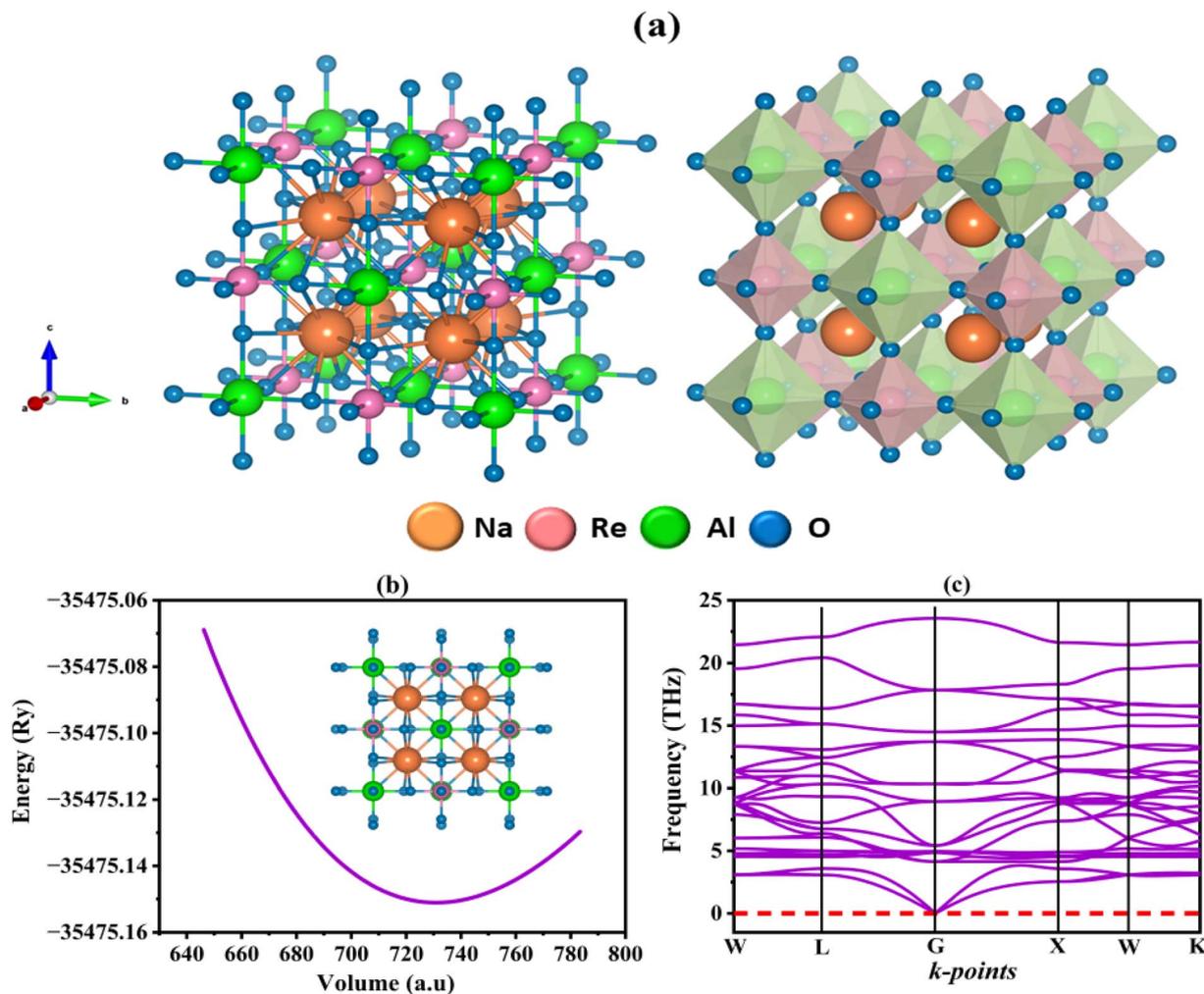| Parameters	Na$_2$ReAlO$_6$
Lattice constant a_0 (Å)	7.57
Ground state volume V_0	730.97
Formation energy E_f (eV per atom)	−3.78
Tolerance factor (τ)	1.02
Octahedral factor (μ)	0.39
Band gap (eV)	1.24

Fig. 1 (a) Optimized crystal structure (b) energy-volume curve (c) phonon dispersion of Na_2ReAlO_6 perovskite.

3.1.2 Dynamic stability. Dynamical stability indicated by the absence of imaginary phonon modes signifies that the crystal structure corresponds to a local minimum on the potential energy surface determined by its internal interatomic interactions. This condition reflects the intrinsic stability of the lattice against small atomic displacements rather than its response to external perturbations.[41] The produced phonon spectra shed light on vibrational properties of material which are demonstrated in Fig. 1(c). The phonon dispersion of Na_2ReAlO_6 exhibits well-defined acoustic and optical branches extending smoothly from the Γ-point up to approximately 25 THz. It should be noted that the present phonon calculations do not include non-analytical corrections related to long-range electrostatic interactions therefore longitudinal optical–transverse optical (LO–TO) splitting at the Γ-point is not explicitly captured. Importantly, no imaginary phonon frequencies are observed across the Brillouin zone, confirming the dynamical stability of the crystal structure. This dynamical stability is essential for maintaining structural stability under operating conditions and supports the suitability of Na_2ReAlO_6 for device-level photovoltaic applications.

3.1.3 Electronic properties. The study of electronic features of material is required to comprehend its potential functioning specifically for optoelectronic, photovoltaic and energy storage applications. Energy band gap (E_g) of substance determines whether it is metallic or semiconducting or insulating.[42]

DFT in conjunction with the Tran-Blaha modified Becke–Johnson potential (TB-mBJ) and PBE-GGA was used to estimate the electronic band structures of Na_2ReAlO_6 double perovskites which are shown in Fig. 2(a). At the Γ symmetry point Na_2ReAlO_6 show semiconducting behavior with direct band gaps value of about 1.243 eV which can facilitate thermal excitation of charge carriers compared to wide bandgap oxide materials. Narrower bandgaps are generally associated with increased intrinsic carrier concentrations under operating conditions which may contribute to improved electrical transport when combined with favorable carrier mobility. The direct band gap of material indicates efficient photon absorption and charge carrier production two crucial properties for optoelectronic and photovoltaic systems. This finding is reliable with the known inverse relationship between band gap energy and lattice
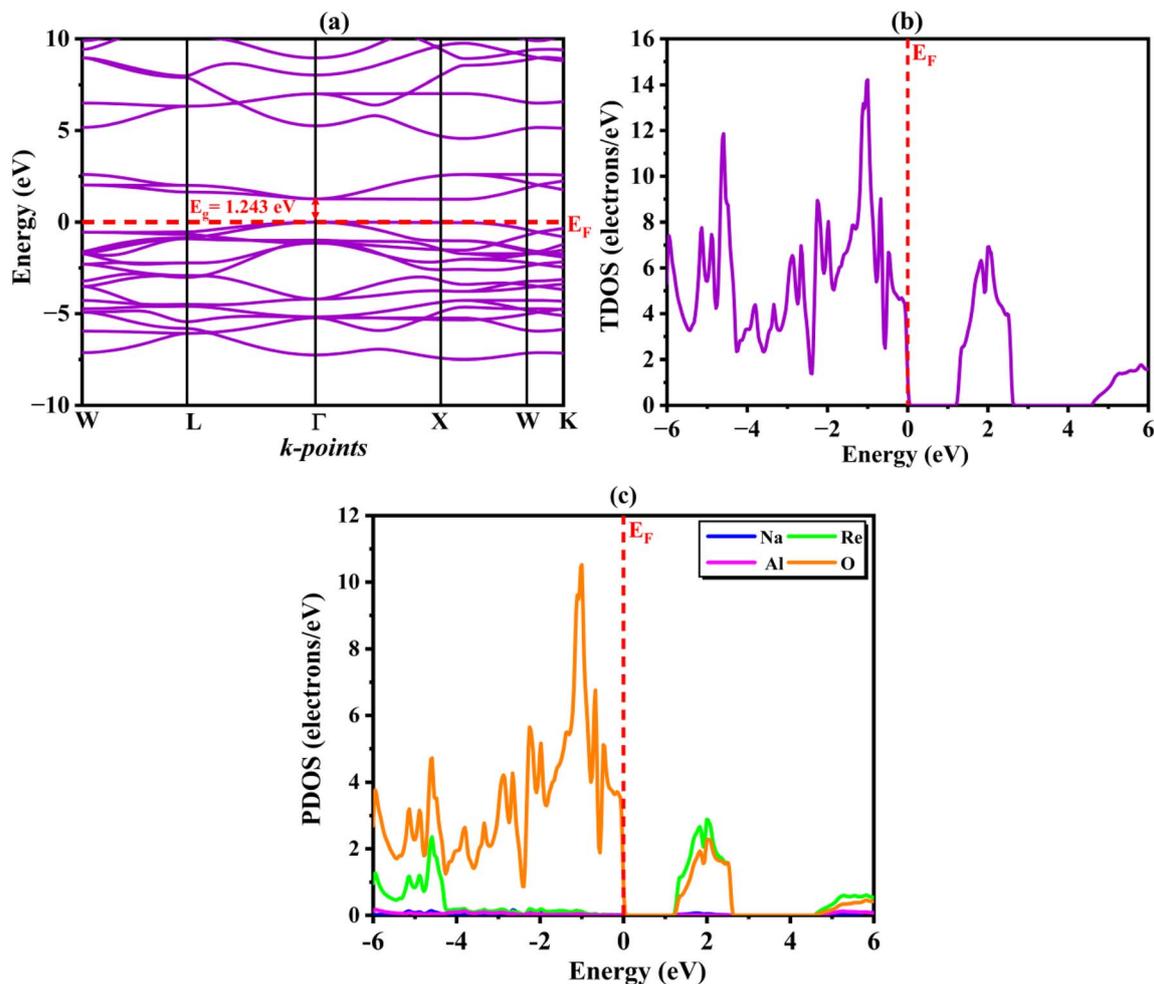
Fig. 2 Computed (a) band structure (b) TDOS and (c) PDOS of Na_2ReAlO_6 perovskite.

constant that has been observed for a number of double perovskite oxides.[43]

To analyze the electronic structure and the orbital contributions near the Fermi level, the total and partial density of states (TDOS and PDOS) were calculated, as shown in Fig. 2(b and c). These results provide insight into the distribution of electronic states and the nature of orbital hybridization which are relevant for interpreting charge transport tendencies but do not directly quantify electrical conductivity.[44] The TDOS plot which exhibit a distinct gap close to the Fermi level (E_F) verify semiconducting nature. For Na_2ReAlO_6 the conduction band is primarily formed from Re-5d states with small contributions from Al-3p orbitals, whereas the valence band which extends from -6 eV to the Fermi level, is primarily made of O-2p states. Near the valence band maximum, a substantial hybridization between the O-2p and Re-5d orbitals is seen, creating a well-connected sp-d hybrid network that strengthens covalent bonds and promotes structural stability. A small amount of Al-p interaction with O-p orbitals is another sign of localized sp hybridization which modifies the charge transport inside the lattice and adjusts the energy band gap. For thermoelectric, optoelectronic and solar applications where effective electron–

hole separation and temperature stability are crucial these characteristics make the Na_2ReAlO_6 a good option for solar cell devices. In this context, the moderate bandgap, strong optical absorption, and temperature-stable electronic behavior predicted for Na_2ReAlO_6 are advantageous for solar cell operation, as these features can support efficient photocarrier generation, effective electron–hole separation, and stable charge transport under operating conditions.[45,46] Similar correlations between bandgap optimization, absorption strength, and thermal robustness have been reported for other oxide-based photovoltaic and optoelectronic materials, further supporting the potential of Na_2ReAlO_6 as a promising absorber material.

3.1.4 Optical properties. An extensive understanding of the interaction between Na_2ReAlO_6 and electromagnetic radiation is provided by the computed optical properties. The material shows a relatively optimum static dielectric constant compared to values typically reported for related perovskite oxide materials in the literature, indicating strong polarization response and effective charge screening under an applied electric field.[47] In addition, a high optical absorption coefficient in the visible region demonstrates efficient photon absorption suitable for solar energy conversion while the calculated optical

conductivity reflects enhanced charge carrier response under optical excitation. The electronic band structure which controls photon–electron interactions and the material reaction to external electromagnetic fields is the direct source of these optical properties. The energy storage (real part ε_1) and energy loss (imaginary part ε_2) of the system under an oscillating electric field are both defined by the complex dielectric function $\varepsilon(\omega) = \varepsilon_1(\omega) + i\varepsilon_2(\omega)$. The following relations were used to generate the real and imaginary components eqn (4) and (5):[48]

$$\varepsilon_1 = 1 + \frac{2}{\pi} M \int_o^\infty \frac{\varepsilon_2(\omega^1)\omega'}{\omega'^2 - \omega^2} d\omega \qquad (4)$$

$$\varepsilon_2(\omega) = \frac{Ve^2}{2\pi\hbar m^2\omega^2} \int d^3k \sum_{nn'} |\langle kn|p|kn'\rangle|^2 f(kn) \times \Big(1 \\ - f\big(kn'\big)\delta\big(E_{kn} - E_{kn'} - \hbar\omega\big)\Big) \qquad (5)$$

The $\varepsilon_1(\omega)$ spectra in Fig. 3(a) (ref. 49) show the polarization ability of Na_2ReAlO_6 when an electromagnetic field is applied. The static dielectric constants ($\varepsilon_1(0)$) of around 6.2 for Na_2ReAlO_6 demonstrated strong polarizability. The notable peaks of the $\varepsilon_1(\omega)$ curves at 2.4 eV represent resonance frequencies linked to interband electronic transitions. The progressive reduction of $\varepsilon_1(\omega)$ beyond this energy confirms that polarization decreases with increasing photon energies. Penn's model which is consistent with the observed inverse connection between dielectric constant and band gap supports the accuracy of the computed results. As shown in Fig. 3(a) (ref. 50) interband transitions have a substantial impact on $\varepsilon_2(\omega)$ which characterizes the photon absorption capabilities. The compound has negligible values below its band gap and its basic transition energies are represented by a strong spike between 2 and 3 eV. Based on the direct semiconducting nature the maximum values of $\varepsilon_2(\omega)$ for Na_2ReAlO_6 are found at approximately 2.9 eV. More photon–electron interaction and improved light absorption efficiency are suggested by the enhanced $\varepsilon_2(\omega)$ response of Na_2ReAlO_6 especially in the visible region (1.8–3.5 eV).

Absorption coefficient that quantifies a material capacity to absorb light provided by eqn (6):[51]

$$\alpha(\omega) = \frac{2\omega k(\omega)}{c} \qquad (6)$$

where $k(\omega)$ is the extinction coefficient. As seen in Fig. 3(b) Na_2ReAlO_6 display a noticeable absorption that starts at 2 eV and varies from the visible spectrum into the ultraviolet. Na_2ReAlO_6 has peak absorption values of approximately 5.4×10^4 cm^{-1} indicating distinct optical transitions and effective photon absorption. These results suggest that Na_2ReAlO_6 could be useful as visible light absorbers in energy conversion devices. Na_2ReAlO_6 is viable for photovoltaic systems because of the significant absorption in the visible region of the maximum peaks matching to photon energy. The stimulated transitions of deep energy electronic states such as the Al-p and Na-s states in the valence band can provide insight into the highest points. Optical conductivity is linked to the imaginary dielectric component by eqn (7).[52]

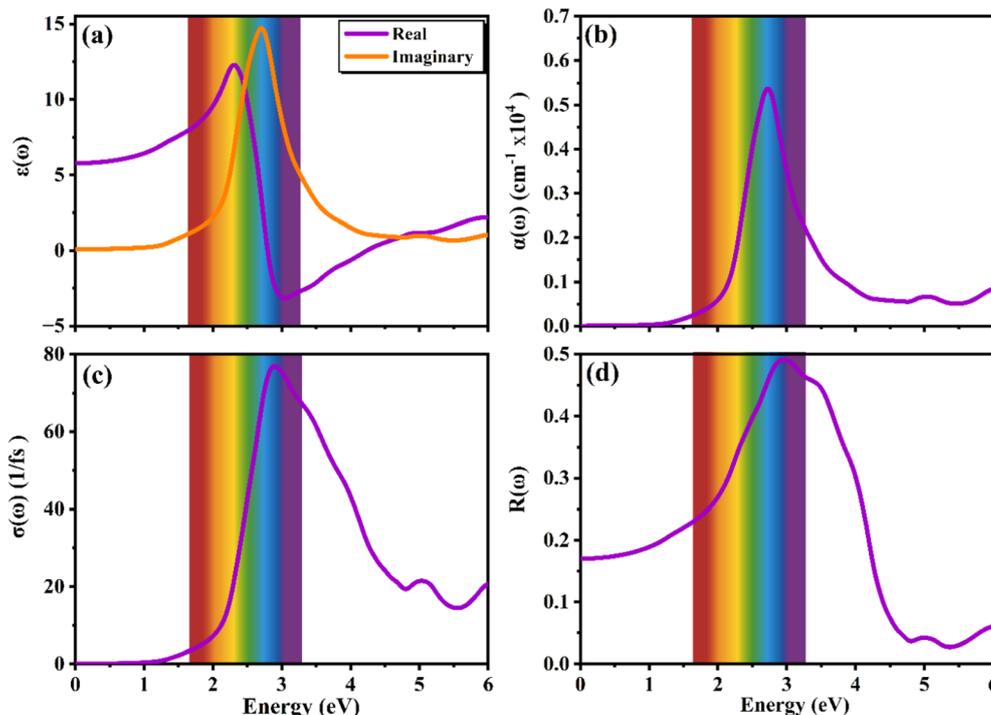$$\sigma(\omega) = \frac{\omega\varepsilon_2(\omega)}{4\pi} \qquad (7)$$

Fig. 3 Optical response (a) dielectric function real and imaginary part (b) absorption coefficient (c) conductivity and (d) reflectivity of Na_2ReAlO_6 perovskite.

The conductivity of Na_2ReAlO_6 peaks between 3 and 3.5 eV which increases around the absorption edge and is low below 2 eV as observed in Fig. 3(c). The maximum optical conductivity values for Na_2ReAlO_6 lies in the visible range. This remarkable reaction increases its potential for integration into optoelectronic systems by confirming good charge carrier mobility after light activation and demonstrating consistency with interband transitions. Material transparency is defined by reflection as mentioned in eqn (8).[53]

$$R(\omega) = \left| \frac{\sqrt{\varepsilon(\omega)} - 1}{\sqrt{\varepsilon(\omega)} + 1} \right|^2 \quad (8)$$

Na_2ReAlO_6 shows low reflectance ($\sim$0.12–0.15) at zero energy signifying excellent infrared transparency (Fig. 3(d)). Reflectivity for Na_2ReAlO_6 steadily rises with photon energy culminating at 0.48 close to 3 eV. Reflectivity gradually drops after this range indicating UV transparency and possible use in solar windows and optical coatings. In the visible region (2–4 eV) of their optical spectra Na_2ReAlO_6 shows notable optical conductivity and dielectric responses with remarkable absorption efficiency.[54] These results show that Na_2ReAlO_6 perovskite oxide is an exciting multifunctional material with prospective uses in solar energy harvesting and optoelectronic devices where regulated light absorption and effective carrier excitation are essential.

3.2 SCAPS-1D analysis

The photovoltaic response of the simulated device structure ITO/ETL/Na_2ReAlO_6/HTL/Anode was examined in detail using SCAPS-1D to understand the influence of different charge transport layers on the overall perovskite solar cell (PSC) performance. ZnS and CSTO were employed as the ETLs each assigned a uniform thickness of 100 nm while Cu_2O was selected as the HTL with a thickness of 100 nm to ensure consistent comparison across the modeled structures. The absorber layer Na_2ReAlO_6 was maintained at a fixed thickness of 800 nm providing sufficient optical absorption for reliable evaluation of charge generation and transport. A schematic representation of the simulated device configuration is presented in Fig. 4. For all simulations the acceptor concentration of the absorber was set to 1×10^{17} cm^{-3} and a defect density of 1×10^{14} cm^{-3} was applied to ensure uniformity across the modeled devices.[55,56] The structures were illuminated under standard AM 1.5G conditions at 1000 mW cm^{-2} replicating real-world solar irradiance while the device temperature was kept at 300 K to reflect common operating environments.[57] The material parameters used for ZnS, CSTO, Na_2ReAlO_6 and Cu_2O are summarized in Table 2.

3.2.1 Energy band alignment. The alignment of the energy bands between the ETLs (ZnS, CSTO) the Na_2ReAlO_6 absorber and the Cu_2O (HTL) plays a pivotal role in dictating charge extraction pathways and interfacial recombination within the device. Achieving a small conduction band offset (CBO) at the ETL/absorber interface is essential for efficient electron injection while a sufficiently large valence band offset (VBO) is required to prevent holes from diffusing back into the ETL. Together these offsets determine the internal carrier dynamics and ultimately influence voltage output, recombination losses and overall power conversion efficiency.[61,62] In this work energy band alignment was evaluated for ZnS and CSTO as potential
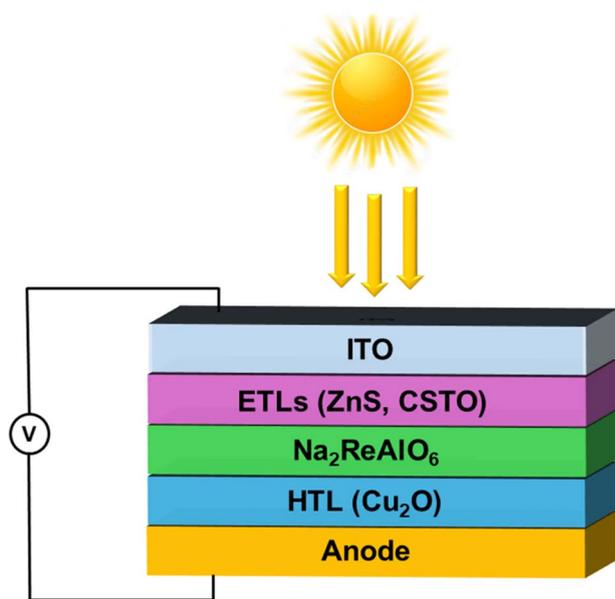

Fig. 4 Schematic illustration of Na_2ReAlO_6-based PSC.

Table 2 Design parameters of the different layers for the simulated device

Parameters	CSTO[58]	ZnS[59]	Na_2ReAlO_6	Cu_2O[60]
Thickness (μm)	0.1	0.1	0.8	0.1
Band gap E_g (eV)	2.96	2.8	1.24	2.20
Electron affinity χ (eV)	3.9	3.8	3.95	3.40
Dielectric permittivity (ε_r)	9	9	6.2	7.50
Effective density of states in CB (cm^{-3})	2.7×10^{19}	2.2×10^{18}	0.10	0.8
Effective density of states in VB	3.5×10^{20}	1.8×10^{19}	2.8	1.24
Electron mobility (cm^2 V^{-1} s^{-1})	6.0×10^3	1×10^2	5.9×10^1	1.0×10^2
Hole mobility (cm^2 V^{-1} s^{-1})	6.6×10^2	2.5×10^1	4.8×10^1	8.6×10^2
Defect type	Neutral	Neutral	Gaussian	Neutral
Energetic distribution	Neutral	Neutral	Neutral	Neutral
Defect density N_d (cm^{-3})	10^{14}	10^{14}	10^{14}	10^{14}

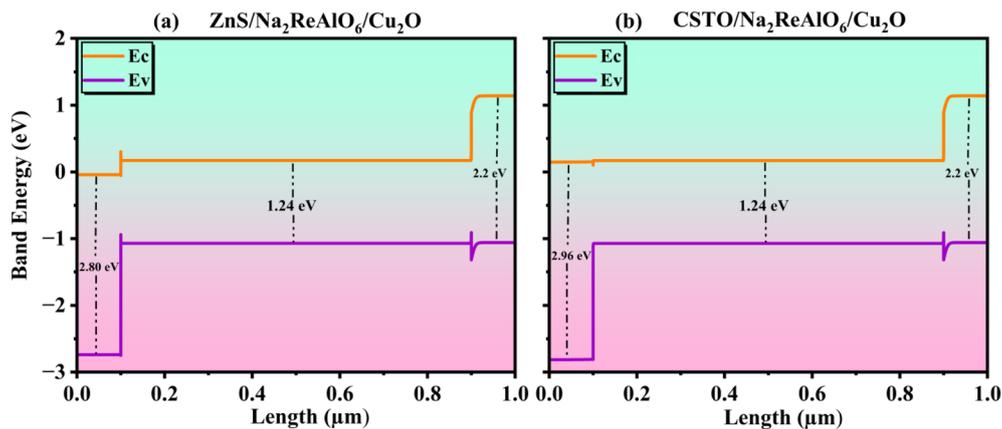**Fig. 5** (a and b) Energy band alignment of Na_2ReAlO_6-based PSCs.

ETLs in combination with Na_2ReAlO_6 and Cu_2O using the standard expressions for CBO and VBO derived from the respective electron affinities and bandgaps of the layers.

The band diagram of the $ZnS/Na_2ReAlO_6/Cu_2O$ (Fig. 5(a)) configuration reveals that ZnS forms a moderately higher conduction band edge relative to the absorber resulting in a small but noticeable barrier for electron transfer. While this offset still permits electron injection it may introduce a slight resistance to transport. In contrast the valence band separation between ZnS and the absorber is pronounced approximately 2.80 eV offering strong hole-blocking capability and effectively minimizing interfacial recombination. This balance of a manageable CBO and a large VBO allows ZnS to operate as a selective ETL albeit with some limitations in electron transport efficiency. For the $CSTO/Na_2ReAlO_6/Cu_2O$ structure as presented in Fig. 5(b) the conduction band edge of CSTO aligns more favorably with the absorber resulting in a smaller CBO and providing a smoother path for electron extraction. The VBO which is approximately 2.96 eV remains sufficiently large to suppress hole migration into the ETL ensuring strong charge selectivity similar to that observed with ZnS. However the reduced electron barrier makes CSTO inherently more suitable for fast electron transport offering an energetically smoother

interface with the absorber. In both configurations the downward step from the absorber's valence band into Cu_2O (2.2 eV) promotes efficient hole extraction while the absorber's bandgap (1.24 eV) remains well-aligned between the ETL and HTL supporting balanced carrier transport throughout the device. The comparative analysis highlights that although both ZnS and CSTO provide strong valence band blocking CSTO exhibits a more favorable conduction band alignment which enhances electron injection and reduces resistive losses. Consequently, CSTO emerges as the more advantageous ETL for enabling efficient charge separation and lower recombination at the Na_2ReAlO_6 interface while ZnS remains a viable but slightly less efficient alternative.

3.2.2 Current density voltage (J–V) characteristics and quantum efficiency (QE). The optoelectronic response of the Na_2ReAlO_6-based solar cells incorporating ZnS and CSTO as ETLs was examined through the simulated J–V and QE characteristics presented in Fig. 6(a and b). As shown in the J–V curves (Fig. 6(a)) both device configurations generate substantial photocurrent under illumination exhibiting nearly linear behavior across most of the bias range which reflects the strong intrinsic absorption of Na_2ReAlO_6 and its ability to suppress bulk recombination. As the voltage approaches the open-circuit

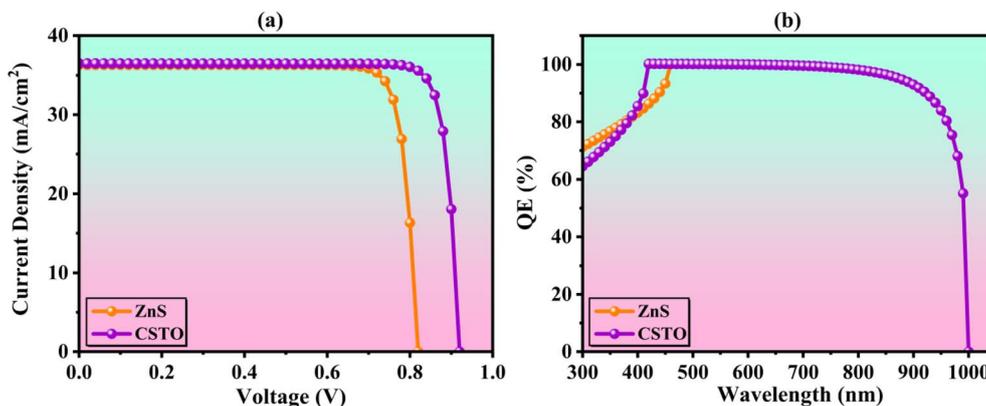**Fig. 6** Depiction of the (a) J–V and (b) QE curve for Na_2ReAlO_6-based PSCs.

region however the differences between the ETLs become more pronounced. The CSTO-based device maintains a higher current density over an extended voltage span indicating more efficient electron extraction and lower interfacial resistance at the CSTO/absorber interface. In contrast the ZnS device begins to show a gradual reduction in current density earlier consistent with the energetic mismatch identified in the band alignment which introduces a slightly larger barrier for electron transport. This smoother extraction pathway in CSTO ultimately supports stronger charge separation and improved device response at higher operating voltages.[63]

These trends are further supported by the spectral quantum efficiency profiles in Fig. 6(b). Both devices demonstrate strong QE in the visible region highlighting the effective absorption and carrier generation capabilities of Na_2ReAlO_6. However the CSTO-containing structure consistently shows higher QE across a broader wavelength range approaching unity in the visible and retaining enhanced response into the near-infrared. This extended spectral activity reflects the reduced recombination probability and more favorable carrier-collection dynamics at the CSTO interface enabling efficient extraction of carriers originating deeper within the absorber. ZnS although capable of achieving high QE in the mid-visible spectrum shows a more pronounced decline beyond 700 nm suggesting reduced collection of long-wavelength generated carriers and higher interfacial recombination losses. The sharper drop near 1000 nm in the ZnS device further underscores this limitation. Overall the combined J–V and QE analyses reveal a coherent picture in which CSTO provides a more compatible and energetically favorable contact to Na_2ReAlO_6 than ZnS. Its superior electron-collection efficiency sustained current density near V_{oc} and broader spectral response collectively translate into a more robust photovoltaic output. These observations not only validate the influence of ETL selection on device performance but also highlight CSTO as a promising candidate for further optimization in oxide-based solar cell architectures.[64]

3.2.3 Influence of the thickness of Na_2ReAlO_6 absorbing layer.

The thickness of the Na_2ReAlO_6 absorber layer plays a central role in defining the operational efficiency of the proposed solar cell as it determines the extent of optical absorption and the subsequent generation and transport of charge carriers. When the absorber is too thin the optical path length becomes insufficient for capturing incident photons across the active spectral range leading to reduced carrier generation.[65] Conversely excessively thick layers introduce longer diffusion paths for photogenerated carriers thereby increasing the probability of bulk recombination.[66] To understand this balance a systematic thickness-dependent simulation was performed for two device configurations ZnS/Na_2ReAlO_6/Cu_2O and CSTO/Na_2ReAlO_6/Cu_2O enabling a comparative assessment of how the ETL influences the behavior of the same absorber. One important photovoltaic metric is the open-circuit voltage (V_{oc}) which is the highest voltage a solar cell can produce while illuminated and no external current is being pulled. It is based on the difference between the quasi-Fermi levels of electrons and holes in the absorber and is heavily impacted by carrier lifetimes, band gaps

and recombination rates. The variation of open-circuit voltage with thickness shown in Fig. 7(a) reveals distinct trends for the two ETLs. ZnS-based devices exhibit a slight rise in V_{oc} as the absorber becomes thicker stabilizing around 0.82 V whereas CSTO-based structure show a gradual decline from nearly 0.95 V to about 0.91 V. This reduction indicates that CSTO provides more competent electron extraction at lower thicknesses and as the absorber thickens the enhanced recombination subtly lowers the attainable V_{oc} despite the material interfacial alignment.

A clearer dependency emerges in the short-circuit current density presented in Fig. 7(b) where both ZnS and CSTO demonstrate a strong increase with absorber thickness. The CSTO configuration achieves J_{sc} values exceeding 36 mA cm^{-2} while ZnS approaches comparable levels at the upper boundary of the simulated range. This behavior directly results from improved optical absorption in thicker Na_2ReAlO_6 layers which capture longer-wavelength photons more effectively particularly in the near-visible region. The fill factor shown in Fig. 7(c) remains relatively stable throughout the thickness variation with CSTO maintaining values above 87% and ZnS slightly lower. Minor fluctuations in FF can be attributed to variations in internal recombination and series resistance as the absorber layer becomes denser. These changes though small illustrate the sensitivity of interfacial transport dynamics to structural modifications within the absorber. The combined impact of these parameters is reflected in the power conversion efficiency depicted in Fig. 7(d). Both device architectures display a substantial improvement in PCE as the absorber thickness increases with CSTO consistently outperforming ZnS. CSTO-based cells surpass 30% efficiency at higher thickness levels whereas ZnS-based devices rise steadily but remain slightly below this benchmark. The prominent efficiency of CSTO arises from its enhanced electron-transport capability and reduced interfacial recombination which allow Na_2ReAlO_6 to fully benefit from the increased photon absorption provided by thicker layers. Overall the trends observed across Fig. 7(a–d) demonstrate that optimizing the thickness of the Na_2ReAlO_6 absorber substantially enhances J_{sc} and PCE with only moderate variations in V_{oc} and FF. Within the studied range up to 1 μm the CSTO/Na_2ReAlO_6/Cu_2O configuration displays a more favorable interplay between optical absorption and carrier extraction marking CSTO as the more effective ETL for achieving high-performance Na_2ReAlO_6-based solar cells.

3.2.4 Effect of absorber defect density.

The influence of absorber defect density on the performance of the Na_2ReAlO_6-based solar cell is substantial as defects serve as active non-radiative recombination sites within the crystal lattice. These defects shorten the lifetime of photogenerated carriers and weaken charge transport ultimately reducing the ability of the device to sustain high photovoltaic output.[67] As shown in Fig. 8(a and b) both device structures display a stable response at lower defect densities (10^{11} to 10^{14} cm^{-3}) where PCE, FF, V_{oc} and J_{sc} remain nearly unchanged. In this region PCE stays close to 25–26% FF remains around 85–86% V_{oc} is maintained near 0.81–0.82 V and J_{sc} is preserved above 36 mA cm^{-2} indicating that the absorber retains efficient optical absorption and charge
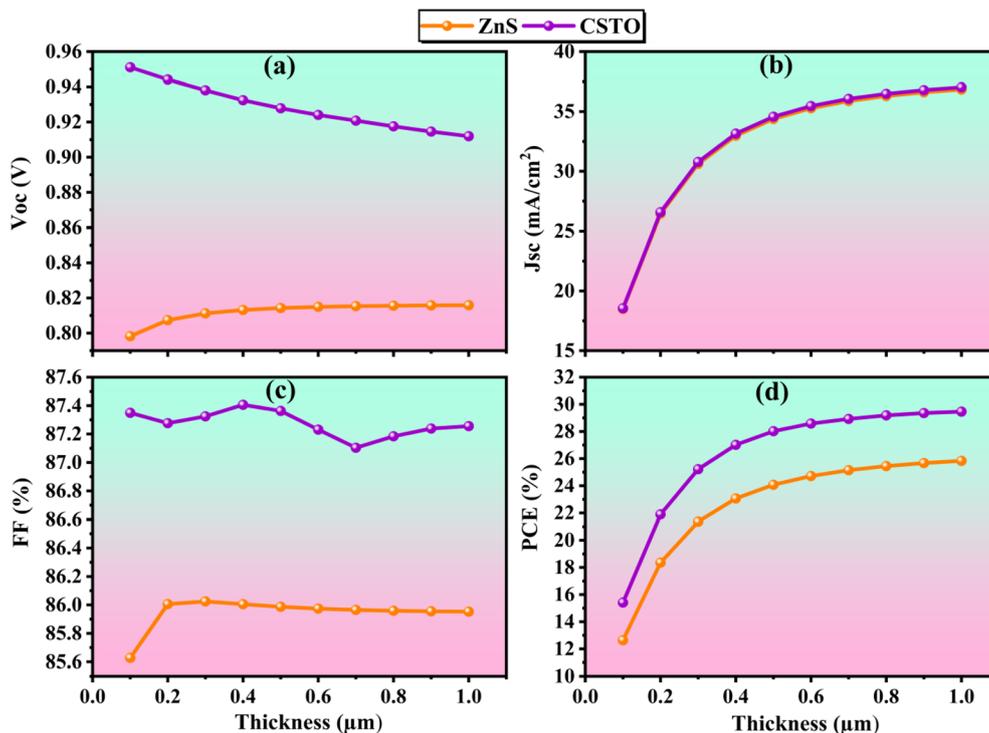
Fig. 7 Impact of absorber thickness variation on the PV performance of Na$_2$ReAlO$_6$-based PSCs: (a) V_{oc} and (b) J_{sc} (c) FF and (d) PCE.

extraction when structural imperfections are minimal. A turning point emerges at a defect density of 10^{15} cm^{-3} where the first noticeable decline begins. At this stage PCE drops slightly from 26% to 24% for both ETLs and FF decreases from 86% to 84% suggesting that recombination pathways start to compete with carrier collection. As the defect density rises further to 10^{16} cm^{-3} performance degradation becomes more pronounced: the PCE for ZnS falls to approximately 17% while CSTO maintains a comparatively higher value of about 18%. Parallel reductions are observed in FF which declines to around 82–83% reflecting the growing influence of defect-assisted charge trapping at deeper energy levels.

The most substantial losses occur at extremely high defect densities (10^{17} to 10^{18} cm^{-3}). At 10^{17} cm^{-3} the PCE of the ZnS-based device collapses to nearly 10% while CSTO retains

a slightly higher output of about 11%. A similar decline is evident in J_{sc} which falls sharply from 35 mA cm^{-2} to nearly 26 mA cm^{-2} and then further down to 17 mA cm^{-2} at 10^{18} cm^{-3}. The V_{oc} also drop from its stable region at 0.81–0.82 V to roughly 0.78 V at 10^{17} cm^{-3} and reaches as low as 0.70–0.72 V at 10^{18} cm^{-3}. These severe reductions confirm that excessive defects dominate the recombination landscape reducing carrier diffusion length and preventing both electrons and holes from reaching the selective contacts. Across all defect concentrations CSTO demonstrates slightly superior photovoltaic performance compared to ZnS primarily due to its stronger charge-transport capability and reduced sensitivity to defect-induced recombination. Fig. 8(a and b) highlights that minimizing intrinsic defects in Na$_2$ReAlO$_6$ is crucial for preserving high device efficiency. Although CSTO provides better tolerance to moderate
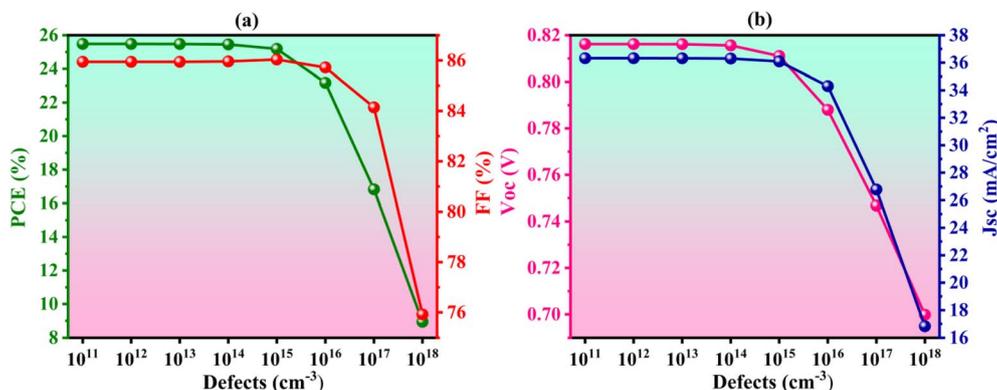

Fig. 8 Effect of absorber defect density on the PV parameters of Na$_2$ReAlO$_6$-based PSCs: (a) PCE and FF (b) V_{oc} and J_{sc}.

defect densities maintaining a low defect concentration remains essential for sustaining high V_{oc} strong photocurrent and overall long-term device stability.

3.2.5 Effect of temperature. Temperature plays a crucial role in determining the operational stability and long-term performance of photovoltaic devices especially under outdoor conditions where thermal fluctuations are unavoidable. The temperature-dependent performance of the Na_2ReAlO_6-based solar cell is evaluated using a fixed device configuration. In this approach temperature is treated as an external parameter within the device model influencing carrier transport, recombination rates and open-circuit voltage while the structural and electronic properties derived from first-principles calculations are assumed to remain unchanged over the investigated temperature range. This approximation is commonly adopted for moderate temperature variations and enables a consistent assessment of temperature-driven trends in photovoltaic performance.[68] A rise in temperature generally accelerates carrier-phonon interactions and enhances recombination ultimately reducing the device's efficiency through an increase in saturation current. The temperature dependence of the Na_2-$ReAlO_6$ solar cell was examined in the range of 300–340 K and the variations in V_{oc}, J_{sc}, FF and PCE are summarized in Fig. 9(a–d). Temperature directly affects carrier recombination, mobility and interfacial transport and these changes are reflected in the device output for both ETLs (ZnS and CSTO) used in combination with the Cu_2O HTL.

In Fig. 9(a) the V_{oc} shows a steady decline as temperature increases. For the ZnS-based device V_{oc} decreases from 0.815 V at 300 K to about 0.785 V at 340 K. The CSTO-based structure maintains a higher V_{oc} across the entire range dropping from approximately 0.915 V to 0.865 V. This reduction is expected as higher temperatures enhance the intrinsic carrier concentration and increase recombination at the absorber/ETL interface. The smaller voltage loss in the CSTO device indicates better thermal stability and reduced interfacial recombination. The J_{sc} remains nearly constant for both designs as illustrated in Fig. 9(b). ZnS shows a stable value around 36.30 mA cm^{-2} while CSTO maintains a slightly higher value near 36.48–36.50 mA cm^{-2} throughout the temperature sweep. The minimal change suggests that photon absorption in Na_2ReAlO_6 and carrier generation are not significantly affected within this moderate temperature range. In parallel a more noticeable temperature influence is observed in the fill factor (FF) shown in Fig. 9(c). For ZnS, FF decreases from 86% at 300 K to nearly 84.2% at 340 K. CSTO again performs better with FF decreasing from 87.2% to about 85.4%. The decline corresponds to higher series resistance and increased carrier-phonon scattering which reduce transport efficiency and raise recombination probability. Moreover the combined impact of reduced V_{oc} and FF results in a gradual decline in PCE shown in Fig. 9(d). For ZnS the efficiency decreases from 26% at 300 K to roughly 24% at 340 K whereas the CSTO device maintains a higher PCE falling from 29.5% to about 27%. The CSTO-based device clearly demonstrates stronger tolerance to thermal effects retaining better charge extraction and lower recombination compared to ZnS.

These analysis demonstrate that the device shows its best performance near 300 K where all parameters V_{oc}, FF and PCE reach their maximum values. Although both ETLs experience thermally induced losses CSTO consistently provides superior
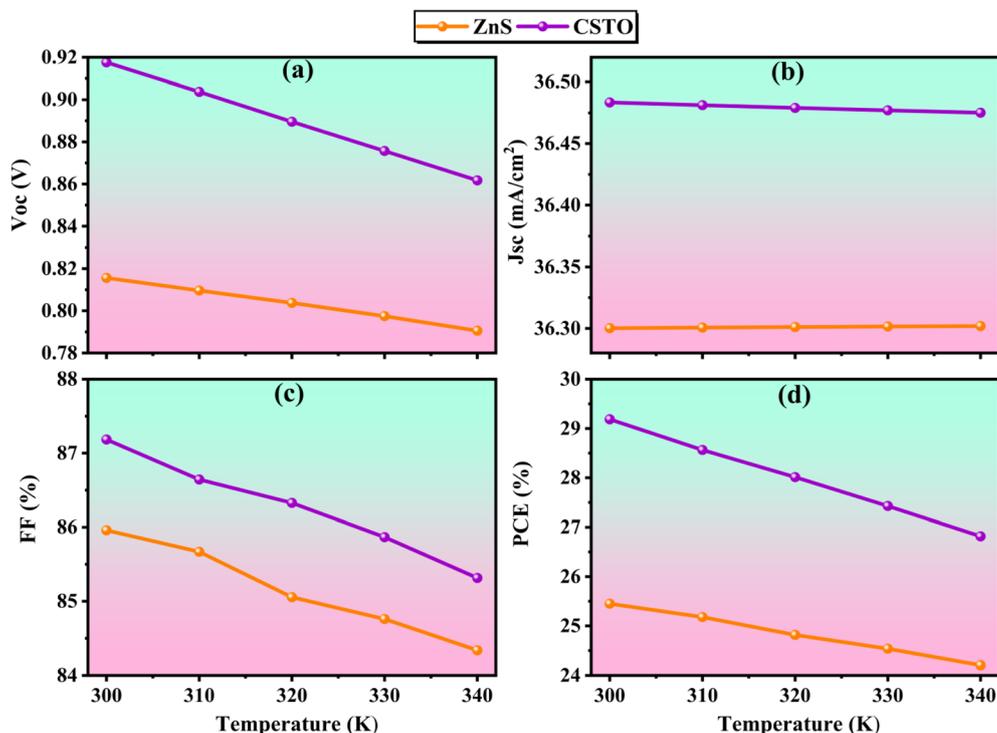

Fig. 9 Temperature effects on the PV parameters of the Na_2ReAlO_6-based PSCs: (a) V_{oc} and (b) J_{sc} (c) FF and (d) PCE.

stability and transport behavior. Across a wide operating temperature range representative of outdoor solar module conditions, CSTO maintains stable band alignment, efficient carrier transport, and reduced recombination losses. This behavior is attributed to its robust oxide lattice, high thermal stability, and limited temperature dependence of key transport parameters. Such characteristics are particularly relevant for real-world photovoltaic operation under fluctuating ambient temperatures and prolonged solar irradiation, where performance degradation is commonly observed. These results indicate that CSTO is a viable temperature-resilient ETL for Na_2ReAlO_6-based solar cells intended for outdoor and high-irradiance applications.

4. Conclusion

In summary, lead-free double perovskites Na_2ReAlO_6 due to their perovskite like structural, electrical and optical characteristics have become attractive options for solar and optoelectronic applications. First-principles calculations with suitable tolerance factors and acceptable negative formation energies and PBE-GGA + TB-mBJ approximation calculations using the Wien2K software all suggest its potential application in practical situations. Evaluation of optical characteristics up to 6 eV of Na_2ReAlO_6 shows notable dielectric constants and absorption coefficients ($\sim 5.4 \times 10^4$ cm^{-1}) with an appropriate band gap of 1.24 eV, making it well suited for solar absorber functionality. Additionally SCAPS-1D simulations is used to quantitatively examine the photovoltaic performance of PSC setups employing Na_2ReAlO_6 as an absorber and ZnS and CSTO were employed as the ETLs while Cu_2O was selected as the HTL to ensure consistent comparison across the modeled structures. Although both ETLs experience thermally induced losses CSTO consistently provides better stability and transport behavior. Na_2ReAlO_6 oxide DPs is a promising candidate for PSCs due to their remarkable photovoltaic properties which include PCE around 29% and QE around 98%. These findings provide clear practical guidance for designing efficient Pb-free PSCs and highlight Na_2ReAlO_6 as a viable absorber material for scalable, stable, and environmentally friendly solar energy technologies.

Conflicts of interest

All authors declare that they have no conflicts of interest.

Data availability

The data that support the findings of this study are available from the corresponding author upon reasonable request.

Acknowledgements

References

1 A. Yadav, *et al.*, Unravelling the role of financial development in shaping renewable energy consumption patterns: insights from BRICS countries, *Energy Strategy Rev.*, 2024, **54**, 101434.

2 S. Yi, *et al.*, Environmental concerns in the United States: can renewable energy, fossil fuel energy, and natural resources depletion help?, *Gondwana Res.*, 2023, **117**, 41–55.

3 U. K. Pata, How to progress towards sustainable development by leveraging renewable energy sources, technological advances, and human capital, *Renewable Energy*, 2025, 122367.

4 N. A. Teli and B. Want, Electronic, magnetic, elastic and optical properties of Ba2CoTaO6 double perovskite oxide: A DFT study, *J. Magn. Magn. Mater.*, 2024, **601**, 172183.

5 S. Ahmed, *et al.*, Recent trends and challenges in lead-free perovskite solar cells: a critical review, *ACS Appl. Energy Mater.*, 2024, **7**(4), 1382–1397.

6 K. Ouali, *et al.*, Electronic structure and optical properties of tin (IV) doped transparent perovskite crystal BaTiO3 for efficient visible optoelectronic devices and solar cells, *Mater. Today Commun.*, 2023, **35**, 106035.

7 M. Z. Kazim, *et al.*, DFT study of optoelectronic and thermoelectric properties of cubic Ba2ZrMO6 (M= Ce, Ti) double perovskites, *J. Solid State Chem.*, 2022, **315**, 123419.

8 M. Khuili, *et al.*, First-principles study of structural, elastic, optoelectronic and thermoelectric properties of B-site-ordered quadruple perovskite Ba4Bi3NaO12, *J. Solid State Chem.*, 2023, **322**, 123955.

9 A. N. Khan, *et al.*, Lead-Free X2MgGeI6 (X= Rb, Cs) Double Perovskites for Multi-functional Energy Applications: A DFT and SCAPS-1D Perspective, *Solid State Sci.*, 2025, 108049.

10 T. Maiti, M. Saxena and P. Roy, Double perovskite (Sr2B′ B″O6) oxides for high-temperature thermoelectric power generation—A review, *J. Mater. Res.*, 2019, **34**(1), 107–125.

11 A. Ayyaz, *et al.*, Optoelectronic and transport response of double perovskites Na2AuMX6 (M= Al, Ga, and X= Br, I) for energy harvesting: A DFT investigation, *Mater. Sci. Eng., B*, 2025, **316**, 118133.

12 L. Hnamte, *et al.*, Electronic and optical properties of double perovskite Ba2VMoO6: FP-LAPW study, in *AIP Conference Proceedings*, AIP Publishing, 2018.

13 R. Ray, *et al.*, Optical and electronic properties of double perovskite Ba2ScSbO6, in *AIP Conference Proceedings*, AIP Publishing, 2016.

14 A. Hossain, *et al.*, An overview of La 2 NiMnO 6 double perovskites: synthesis, structure, properties, and applications, *J. Sol-Gel Sci. Technol.*, 2020, **93**, 479–494.

15 J. A. Abraham, *et al.*, A comprehensive DFT analysis on structural, electronic, optical, thermoelectric, SLME properties of new Double Perovskite Oxide Pb2ScBiO6, *Chem. Phys. Lett.*, 2022, **806**, 139987.

16 A. N. Khan, *et al.*, Lead-free, stable, and effective double Ca2TiXO6 (X= Ge, Sn) perovskites for photovoltaic application, *J. Sol-Gel Sci. Technol.*, 2025, 1–13.

17 M. Retuerto, *et al.*, Half-metallicity in Pb2CoReO6 double perovskite and high magnetic ordering temperature in Pb2CrReO6 perovskite, *Chem. Mater.*, 2015, **27**(12), 4450–4458.

18 M. Tanzeel, *et al.*, A computational investigation of novel double perovskite oxides Ba2XReO6 (X= Li, Na) for optoelectronic and photocatalytic applications, *Int. J. Mod. Phys. B*, 2025, 2650012.

19 M. M. Stanley, J. N. Baby and M. George, Alkali metal-based tantalates ATaO3 (A= Na And K) decorated on functionalized carbon nanofiber employed as an electrocatalyst: An effective A-site variants for electrochemical sensing of antiviral drug in environmental samples, *J. Environ. Chem. Eng.*, 2024, **12**(6), 114896.

20 A. Kausar, *et al.*, Advent of alkali metal doping: a roadmap for the evolution of perovskite solar cells, *Chem. Soc. Rev.*, 2021, **50**(4), 2696–2736.

21 M. T. Iqbal, *et al.*, Next-generation materials discovery using DFT: functional innovation, *Scholars J. Eng. Technol.*, 2025, **7**, 454–486.

22 W. Kohn and L. J. Sham, Self-consistent equations including exchange and correlation effects, *Phys. Rev.*, 1965, **140**(4A), A1133.

23 P. Hohenberg and W. Kohn, Inhomogeneous electron gas, *Phys. Rev.*, 1964, **136**(3B), B864.

24 E. Sjöstedt, L. Nordström and D. Singh, An alternative way of linearizing the augmented plane-wave method, *Solid State Commun.*, 2000, **114**(1), 15–20.

25 J. P. Perdew, Generalized gradient approximation made simple, *Phys. Rev. Lett.*, 1997, **77**, 3868.

26 F. Tran and P. Blaha, Accurate band gaps of semiconductors and insulators<? format?> with a semilocal exchange-correlation potential, *Phys. Rev. Lett.*, 2009, **102**(22), 226401.

27 R. di Meo, *et al.*, Calculation of phonon dispersions on the grid using Quantum ESPRESSO. Proc. COST School (Trieste), 2009.

28 P. Giannozzi, *et al.*, Advanced capabilities for materials modelling with QUANTUM ESPRESSO, *J. Phys.: Condens. Matter,*, 2017, **29**(46), 465901.

29 M. Z. Abbasi, *et al.*, Enhancing the performance of lead-free CsInCl3 perovskite solar cells with Ag and Au plasmonic nanoparticles: A DFT and SCAPS-1D analysis, *Results Eng.*, 2025, 105043.

30 A. Ayyaz, *et al.*, Investigation of optoelectronic and photovoltaic characteristics of A2NaAlI6 (A= Rb, Cs)-based perovskite solar cells with different charge transport layers: DFT and SCAPS-1D simulation, *Sol. Energy*, 2025, **299**, 113738.

31 M. Z. Kazim, *et al.*, Physical properties of Ba2XIO6 (X= Ag, Na) double perovskite oxides for energy harvesting devices, *Arabian J. Sci. Eng.*, 2023, **48**(1), 779–787.

32 M. Kaleem, M. M. A. Iqbal and A. N. Khan, Stability and hydrogen storage performance of Na 2 LiXH 6 (X= Zr, V, Cr) double perovskite hydrides via DFT and AIMD, *RSC Adv.*, 2026, **16**(2), 995–1007.

33 E. K. Albrecht and A. J. Karttunen, Investigation on the predictive power of tolerance factor τ for A-site double perovskite oxides, *Dalton Trans.*, 2023, **52**(35), 12461–12469.

34 Z. Li, *et al.*, Stabilizing perovskite structures by tuning tolerance factor: formation of formamidinium and cesium lead iodide solid-state alloys, *Chem. Mater.*, 2016, **28**(1), 284–292.

35 M. M. A. Iqbal, *et al.*, Quantum chemical investigation of A2LiBiI6 perovskites with Na, K, and Rb for photocatalytic water-splitting application, *npj Clean Energy*, 2026, **2**(1), 1.

36 W. Li, *et al.*, Can we predict the formability of perovskite oxynitrides from tolerance and octahedral factors?, *J. Mater. Chem. A*, 2013, **1**(39), 12239–12245.

37 L. Feng, *et al.*, Formability of ABO3 cubic perovskites, *J. Phys. Chem. Solids*, 2008, **69**(4), 967–974.

38 A. Talapatra, *et al.*, A machine learning approach for the prediction of formability and thermodynamic stability of single and double perovskite oxides, *Chem. Mater.*, 2021, **33**(3), 845–858.

39 M. A. Ullah, *et al.*, An approach towards next-generation hydrogen storage: a DFT study on A 2 LiTiH 6 (A= K, Ca) perovskite hydrides, *RSC Adv.*, 2025, **15**(46), 38714–38728.

40 S. J. Mole, X. Zhou and R. Liu, Density functional theory (DFT) study of enthalpy of formation. 1. Consistency of DFT energies and atom equivalents for converting DFT energies into enthalpies of formation, *J. Phys. Chem. Lett.*, 1996, **100**(35), 14665–14671.

41 F. Togo, *et al.*, Attention network test: assessment of cognitive function in chronic fatigue syndrome, *J. Neuropsychol.*, 2015, **9**(1), 1–9.

42 J. Gusakova, B. K. Tay and V. Gusakov, General approach for band gap calculation of semiconductors and insulators, *Phys. Status Solidi*, 2016, **213**(11), 2834–2837.

43 U. A. Khan, *et al.*, First-principles investigation on the structural, electronic, mechanical and optical properties of silver based perovskite AgXCl3 (X= Ca, Sr), *J. Mater. Res. Technol.*, 2022, **20**, 3296–3305.

44 M. I. Hussain and R. A. Khalil, Density functional theory studies of the structural, optoelectronic, bond stiffness and lattice dynamical properties of double perovskite oxides M2YVO6 (M= Mg, Sr): Promising candidates for optoelectronic applications, *Mater. Sci. Semicond. Process.*, 2022, **152**, 107050.

45 M. Tanzeel, *et al.*, A computational investigation of novel double perovskite oxides Ba2XReO6 (X= Li, Na) for optoelectronic and photocatalytic applications, *Int. J. Mod. Phys. B*, 2026, **40**(03), 2650012.

46 S. Kanwal, *et al.*, Exploring the Effect of Cerium Doping on the Physical Properties of Bi2Ca2-xCexCoO6 Double Perovskite Oxides: Experimental and Theoretical Insights, *Solid State Sci.*, 2025, 108189.

47 C. Homes, *et al.*, Optical response of high-dielectric-constant perovskite-related oxide, *science*, 2001, **293**(5530), 673–676.

48 K. Ullah, *et al.*, Structural, Optical, Thermal, and Dielectric Properties of the Double Perovskite Sr2FeMoO6 for Wireless Applications, *Ceram. Int.*, 2025, 48644–48654.

49 A. Kuzmenko, Kramers–Kronig constrained variational analysis of optical spectra, *Rev. Sci. Instrum.*, 2005, **76**(8), 083108.

50 R. Eibler, M. Dorrer and A. Neckel, Calculation of the imaginary part $\in 2$ (ω) of the dielectric function for TiN and ZrN, *J. Phys. C: Solid State Phys.*, 1983, **16**(16), 3137.

51 D. Pattanayak, *et al.*, Optical and transport properties of new double perovskite oxide, *J. Mater. Sci.: Mater. Electron.*, 2018, **29**(8), 6215–6224.

52 R. Mukherjee, *et al.*, Micro-structure, optical properties and ac conductivity of rare earth double perovskite oxides: Sr2ErNbO6, *Phys. B*, 2013, **422**, 78–82.

53 Q. Dai, *et al.*, Physical properties of novel double perovskite oxides Ba2XSbO6 (X= P, As) by first-principle calculations, *Chem. Phys.*, 2024, **586**, 112392.

54 V. Udhayasuriyan, *et al.*, Enhanced Energy Harvesting of Novel Gd_2FeCrO_6 Double Perovskite Hydroelectric Cells with Sustained Voltage Discharge, *Mater. Res. Bull.*, 2025, 113783.

55 A. Pradhan, P. Subudhi and D. Punetha, Enhancing photovoltaic performance in copper-based perovskites: A comparative analysis of 3D and 2D structural paradigms for superior efficiency, *J. Power Sources*, 2025, **629**, 235999.

56 S. Ullah, *et al.*, Optimization of Mixed Valence Cs2Au2I6-based Double Perovskite Solar Cells by SCAPS-1D Simulation, *J. Phys. Chem. Solids*, 2025, 113192.

57 M. D. Haque, *et al.*, Numerical analysis for the efficiency enhancement of MoS2 solar cell: a simulation approach by SCAPS-1D, *Opt. Mater.*, 2022, **131**, 112678.

58 M. Mahmood, *et al.*, Advancing perovskite solar cells: Unveiling the superior efficiency of copper-doped Strontium Titanate as a novel ETL, *Sol. Energy*, 2024, **279**, 112806.

59 D. Dou, *et al.*, Perovskite-based indoor photovoltaics and their competitors, *Adv. Funct. Mater.*, 2024, **34**(13), 2314398.

60 H. Kuang and Y. Xiao, Numerical simulation of Cu2Te based thin film solar cell with Cu2O HTL for high efficiency, *Micro Nanostruct.*, 2024, **188**, 207790.

61 M. Noman, *et al.*, Optimizing band gap, electron affinity, & carrier mobility for improved performance of formamidinium lead tri-iodide perovskite solar cells, *Mater. Sci. Eng., B*, 2024, **300**, 117114.

62 A. Ayyaz, *et al.*, Investigation of promising stable halide double perovskites K2LiXI6 (X= Al, Ga) for solar cells and thermoelectric device applications: DFT and SCAPS-1D simulation approach, *Chem. Phys. Lett.*, 2025, 142433.

63 Y. Li, *et al.*, Open-Circuit Voltage Loss Management for Efficient Inverted Wide-Bandgap Perovskite Photovoltaics, *Adv. Funct. Mater.*, 2025, **35**(7), 2415331.

64 A. N. Khan, *et al.*, Multi-functional DFT and SCAPS-1D analysis of lead-free Z2MgGeI6 (Z= Na, K) double perovskites for optoelectronic, photo-catalytic, and photovoltaic applications, *Sol. Energy Mater. Sol. Cells*, 2026, **294**, 113922.

65 D. N. Q. Agha and Q. T. Algwari, The influence of the interface layer between the electron transport layer and absorber on the performance of perovskite solar cells, in *IOP Conference Series: Materials Science and Engineering*, IOP Publishing, 2021.

66 M. Noman, A. D. Khan, and S. T. Jan, Influence of absorber layer thickness and band gap tuning on the optical and electrical properties of semi-transparent flexible perovskite solar cells, in *Advances in Clean Energy Systems and Technologies*, Springer, 2024, p. 23–31.

67 S. T. Jan and M. Noman, Influence of layer thickness, defect density, doping concentration, interface defects, work function, working temperature and reflecting coating on lead-free perovskite solar cell, *Sol. Energy*, 2022, **237**, 29–43.

68 A. Dhass, Y. Prakash and K. Ramya, Effect of temperature on internal parameters of solar cell, *Mater. Today: Proc.*, 2020, **33**, 732–735.